

# Atomic Scale Measurement of Polar Entropy

Debangshu Mukherjee,<sup>1</sup> Sergei Prokhorenko,<sup>2,3</sup> Leixin Miao,<sup>1</sup> Ke Wang,<sup>4</sup> Eric Bousquet,<sup>2</sup> Venkatraman Gopalan,<sup>1,4</sup> and Nasim Alem<sup>1,4,\*</sup>

<sup>1</sup>*Department of Materials Science and Engineering, The Pennsylvania State University, University Park, Pennsylvania 16802, USA*

<sup>2</sup>*Theoretical Materials Physics Q-MAT CESAM, University of Liège, Sart Tilman B-4000, Belgium*

<sup>3</sup>*Physics Department and Institute for Nanoscience and Engineering,  
University of Arkansas, Fayetteville, Arkansas 72701, USA*

<sup>4</sup>*Materials Characterization Laboratory, Materials Research Institute,  
The Pennsylvania State University, University Park, Pennsylvania 16802, USA*

(Dated: July 18, 2018)

Entropy is a fundamental thermodynamic quantity that is a measure of the accessible microstates available to a macroscopic system. Quantitative measurements of entropy change using calorimetry are predominantly macroscopic, with direct atomic scale measurements being exceedingly rare. Here for the first time, we experimentally quantify polar configurational entropy (in meV/K) using sub-ångström resolution aberration corrected scanning transmission electron microscopy. This is performed in a single crystal of the prototypical ferroelectric  $\text{LiNbO}_3$  through the quantification of the niobium and oxygen atom column deviations from their paraelectric positions with a precision of  $\sim 2 \text{ pm}$ . Combined with first principles theory plus mean field effective Hamiltonian methods, we demonstrate that the intrinsic entropic contribution dominates the experimentally measured entropy. Significant excursions of the polarization away from its symmetry constrained direction is seen in single domain regions which increases in the proximity of domain walls. Excellent agreement between our experimentally measured and theoretically predicted entropy values is observed. This study presents a powerful tool to quantify absolute entropy on the atomic scale and demonstrates its dominant role in local symmetry breaking at finite temperatures in classic, nominally Ising ferroelectrics.

Subject Areas : Condensed Matter Physics, Materials Science, Statistical Physics

## I. INTRODUCTION

While absolute entropy, a fundamental thermodynamic parameter, is difficult to experimentally measure macroscopically, a change in entropy ( $\Delta S = \frac{\Delta Q_{\text{rev}}}{T}$ ), is usually measured using calorimetry, where  $\Delta Q_{\text{rev}}$  is the reversible heat supplied to the system at a constant temperature  $T$ [1, 2]. At absolute zero ( $T = 0\text{K}$ ), the total entropy of a perfect crystal free of dopants is zero[3]. Upon addition of reversible heat to the system, the entropy increases. Directly measuring the absolute entropy of the system through characterizing the microscopic configurations, or the microstates, is challenging. For example, even for a mole of matter consisting of Avogadro's number of molecules ( $N \approx 6 \times 10^{23}$ ), the total possible number of equiprobable microstates at equilibrium, ( $W \approx e^N$ ) is larger than the number of atoms in the observable universe[4]. Such enormously large numbers of microstates are also involved in condensed matter systems where a dopant atom may choose any one of equivalent atomic sites in a periodic lattice. Modern microscopy techniques such as scanning transmission electron microscopy(STEM) and scanning tunneling microscopy (STM) are able to directly image microstates on an unprecedented length scale with precision approaching a single picometer[5–7]. However, converting these images into quantitative measures of entropy (in meV/K) is exceedingly rare, for example, as in a recent example of finding configurational entropy in a single molecule of dibutyl sulfide (with 27 atoms in the formulae unit) using STM[8]. In condensed matter, we know of no other examples where atomic resolution

microscopy, and in particular STEM has been used to quantify entropy.

In this study, we probe a single crystal of ferroelectric  $\text{LiNbO}_3$ , a well-known optical ferroelectric, to measure the polar entropy using aberration-corrected (AC) STEM[9]. Ferroelectric materials have a spontaneous and switchable electrical polarization, which is a consequence of the lattice distortions in the crystal structure that break inversion symmetry[10–12]. Regions of uniform polarization are called domains, with the boundary between two adjacent domains called a domain wall[13–16]. Since the ferroelectric polarization is a consequence of crystal distortions, the possible polar vectors can occur only along certain symmetry allowed crystallographic directions. As a uniaxial displacive ferroelectric (space group R3c), the origin of the spontaneous polarization in  $\text{LiNbO}_3$  is a consequence of the niobium and lithium cation displacements with respect to the oxygen octahedral center along either the (0001) or the (000̄1) crystallographic axes, and thus the polarization vectors are restricted to only  $\langle 0001 \rangle$  direction (also labeled as z- or 3- direction)[9, 17–20]. Classical uniaxial ferroelectrics such as  $\text{LiNbO}_3$  have been long thought of as Ising like, since lattice distortions away from the symmetry restricted polarization directions has a high energy cost associated with them[10, 14]. However, recent research have pointed out that fluctuations away from the Ising polarization direction do exist in ferroelectrics, with Bloch and Néel components arising at domain walls, which were predicted and also experimentally detected[21–24].

In this work, however, we show using first principles theory plus mean field effective Hamiltonian methods that non-Ising polar fluctuations are intrinsic to ferroelectric  $\text{LiNbO}_3$  at finite temperatures, and that they exist even in a homoge-

\* alem@matse.psu.edu

neous lattice with no domain walls. Using ultrahigh resolution AC-STEM, we experimentally quantify this fluctuation generated entropy on the atomic scale for the first time by determining the Nb and O positions with a precision approaching  $\sim 2\text{pm}$ . The precise composition of the chosen crystal is  $\text{Li}_{0.95}\text{Nb}_{1.01}\text{O}_3$  (also referred to as the congruent composition or CLN where crystal growth is easy to perform)[25–29]. This off-stoichiometry leads to the presence of Li vacancies and  $\text{Nb}_{\text{Li}}$  antisites that will contribute to extrinsic polar entropy. We estimate the structural energy and intrinsic entropy of stoichiometric  $\text{LiNbO}_3$  through theory, and by comparison with the experimental measurement of the polar entropy, demonstrate that even inside a bulk domain in the congruent composition intrinsic entropy is dominant (>80% of the total measured entropy). We observe that the extrinsic entropy contribution increasing by  $\sim 25\%$  as we get closer to the domain walls, but still not the predominant contribution. The entropy manifests itself as symmetry fluctuations of the polarization perpendicular to the  $\langle 0001 \rangle$  polar axis, leading to local non-Ising behavior. It is shown that entropic decrease in overall energy dominates any increase in electrostatic energy due to these non-Ising fluctuations. The study thus presents an absolute measurement of polar entropy, its spatial mapping with atomic scale resolution, and insights in terms of local symmetry breaking.

## II. EXPERIMENTAL SETUP

We used ultra high resolution scanning transmission electron microscopy to image the oxygen and niobium atom columns to determine the polarization metrology through quantification of both the niobium and oxygen atom positions. To visualize the atom positions, at the  $180^\circ$  domain wall and also at the bulk domain, we imaged the electron transparent  $\text{LiNbO}_3$  sample from the  $[1\bar{1}00]$  crystallographic zone axis which enables the displacements to lie in plane, with the sample preparation details expanded in detail in section IV A. While both bright field (BF) and annular dark field (ADF) STEM images were acquired (Figure 1a and Figure 1b), we exclusively use BF-STEM images for the quantification of polar displacements since both the niobium and oxygen atom positions and their relative displacements can be quantified. This technique has been previously demonstrated as a viable pathway for the determination of the cation and oxygen atom positions simultaneously[30, 31], and is less susceptible to specimen tilt and defocus in comparison to annular bright field (ABF)-STEM[32, 33]. The total polar displacements are calculated on a unit cell basis, with respect to a mean unit cell calculated from the entire image (Figure 1c). As demonstrated in Figure 1d, displacements along  $\langle 0001 \rangle$  are the Ising displacements, while those along  $\langle 11\bar{2}0 \rangle$  are the Néel displacements. From a symmetry perspective, since  $\text{LiNbO}_3$  is a uniaxial ferroelectric, the only polar niobium-oxygen displacements in bulk domain may be expected to be Ising.

After imaging the atom columns, we used custom-developed MATLAB scripts to refine the positions for sub-pixel precision displacement metrology. To perform the re-

finement, we started by locating the highest intensity spots as a first pass to estimate atom positions in ADF-STEM and inverted contrast BF-STEM images. We performed subsequent refinement by fitting a multi-peak two-dimensional Gaussian to the observed atom intensity distribution to get the atom positions with a precision approaching  $\sim 2\text{pm}$ [34]. To determine the polar displacements, we first assigned the refined atom positions to their corresponding  $\text{LiNbO}_3$  unit cell values, and then generated an average unit cell by summing all the individual unit cells throughout the BF-STEM image (Figure 1d). The dimensions of this calculated average unit cell (Figure 1d) closely matches with the reported structure of  $\text{LiNbO}_3$ [35, 36], indicating the high degree of precision of the obtained BF-STEM images. The oxygen and niobium centers of mass for each individual unit cell (Figure 1e) were subsequently compared to the center of the calculated average unit cell to determine the polar displacements for both niobium and oxygen atoms. The relative Nb-O polar displacement vectors were then measured by subtracting the oxygen displacement vector from the niobium displacement vector in each unit cell. Thus, the average unit cell that we used for the individual niobium and oxygen displacements acts as the basis, and since a common basis is used for both the atom positions, the final relative displacement is independent of the choice of the reference. Using this procedure, we thus successfully calculated a polar vector for each unit cell in a BF-STEM image (Figure 1e), which was subsequently decomposed into its corresponding Ising and Néel components along the  $\langle 0001 \rangle$  and  $\langle 11\bar{2}0 \rangle$  directions respectively.

## III. RESULTS AND DISCUSSIONS

To visualize the spatial evolution of the niobium-oxygen polar displacements, we applied our displacement metrology as detailed in section II to a section of the  $180^\circ$  domain wall, with Figure 2a demonstrating the corresponding BF-STEM image, where the scaled Ising displacements are overlaid. The blue regions refer to Ising displacements along  $[000\bar{1}]$  axis, while the red regions indicate the Ising displacements along the  $[0001]$  direction. The  $180^\circ$  nature of the wall and the domain reversal across only one to two unit cells could be immediately ascertained, with the non-ideal behavior of the wall being apparent through the presence of local kinks and bends. The canonical polarization transitions to zero at the wall, with the wall width being approximately one to two unit cells, similar to the previously observed polarization behavior of niobium atoms across the  $180^\circ$  wall[37]. Plotting the individual Ising displacements, we observe that the displacements across the domain wall are associated with simultaneous motion of both the niobium and the oxygen centers.

The domain wall and its vicinity are also characterized by regions of Néel displacements, i.e. polar displacements perpendicular to the wall, with parts of the wall featuring higher Néel intensities compared to the neighboring domain (Figure 2b). In contrast to the Ising displacements, which are driven by the cooperative motion of oxygen and niobium atoms across the domain wall, the Néel displacements are however primarily

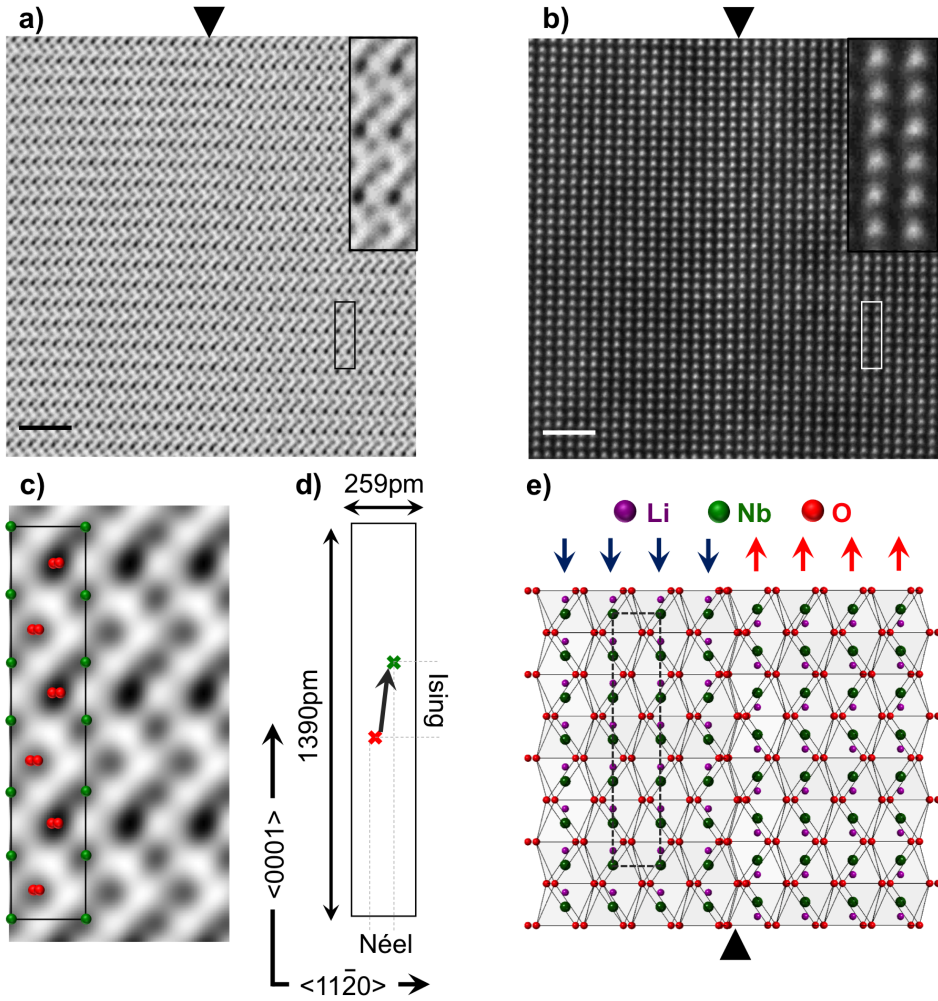


**FIG. 1. Schematic of electron microscopy experiments.** (a) Aberration-corrected Bright Field (BF)-STEM image of a domain wall in  $\text{LiNbO}_3$ , with the wall location marked by the black triangle, with a zoomed section in inset showing oxygen and niobium positions. Scale bar is 2nm. (b) Simultaneously collected Annular Dark Field (ADF)-STEM image of the region imaged in Figure 1a, with the wall location marked by the black triangle. The zoomed section in inset shows the niobium atoms. Scale bar is 2nm. (c) Averaged mean unit cell from the experimental datasets with the niobium positions in green and the oxygen atoms in red. The unit cell is shown as the black rectangle. (d) The schematic of the unit cell with the experimentally measured long and short dimensions. The niobium and oxygen centers are shown as green and red crosses with the projected Ising and Néel displacement directions. (e) Atomic model of  $\text{LiNbO}_3$  crystal structure viewed from the  $[1\bar{1}00]$  zone axis, with lithium atoms in purple, niobium atoms in green and oxygen atoms in red. The average unit cell for polarization calculations is shown as a black dashed box with the arrows referring to the polarization direction.

driven by the niobium atoms reaching a maxima in magnitude at the wall.

From the Ising and Néel displacements which we map in Figure 2a and Figure 2b respectively, it is obvious that contrary to the classical expectation of a pure Ising wall, non-Ising displacements do in fact occur. To visualize their combined effect, we calculated the curl of the polar niobium-oxygen displacement vector ( $\nabla \times \vec{u}_{\text{Nb-O}}$ ), which is plotted in Figure 2c. The magnitude of the curl increases at the wall, indicating clockwise rotation of the polar Niobium-Oxygen displacement vector at the wall. The Néel displacements however at the domain wall have a directional preference, which may be due to the higher electrostatic energy needed for head-to-head or tail-to-tail configurations arising from bidirectional Néel

displacements.

Figure 2d shows the statistical averages of the total Ising and Néel polar displacements along the  $\langle 0001 \rangle$  direction. We observe that the classical Ising displacement profile with a magnitude reversal of approximately 55pm, matching closely with theoretical predictions[9, 19]. Conversely, the wall is also associated with approximately 10pm of Néel displacements, centered at the wall. Such non-Ising displacements have been predicted before, though one may not expect them in a hard uniaxial ferroelectric[15, 18, 38]. Previous experimental observations of the polarization vector deviating from the bulk polar axis have been observed in  $\text{PbTiO}_3$ ,  $\text{LiTaO}_3$  and  $\text{PbZr}_x\text{Ti}_{1-x}\text{O}_3$ , but not in  $\text{LiNbO}_3$ [5, 23, 39].

To understand the origin of the polar instability leading to

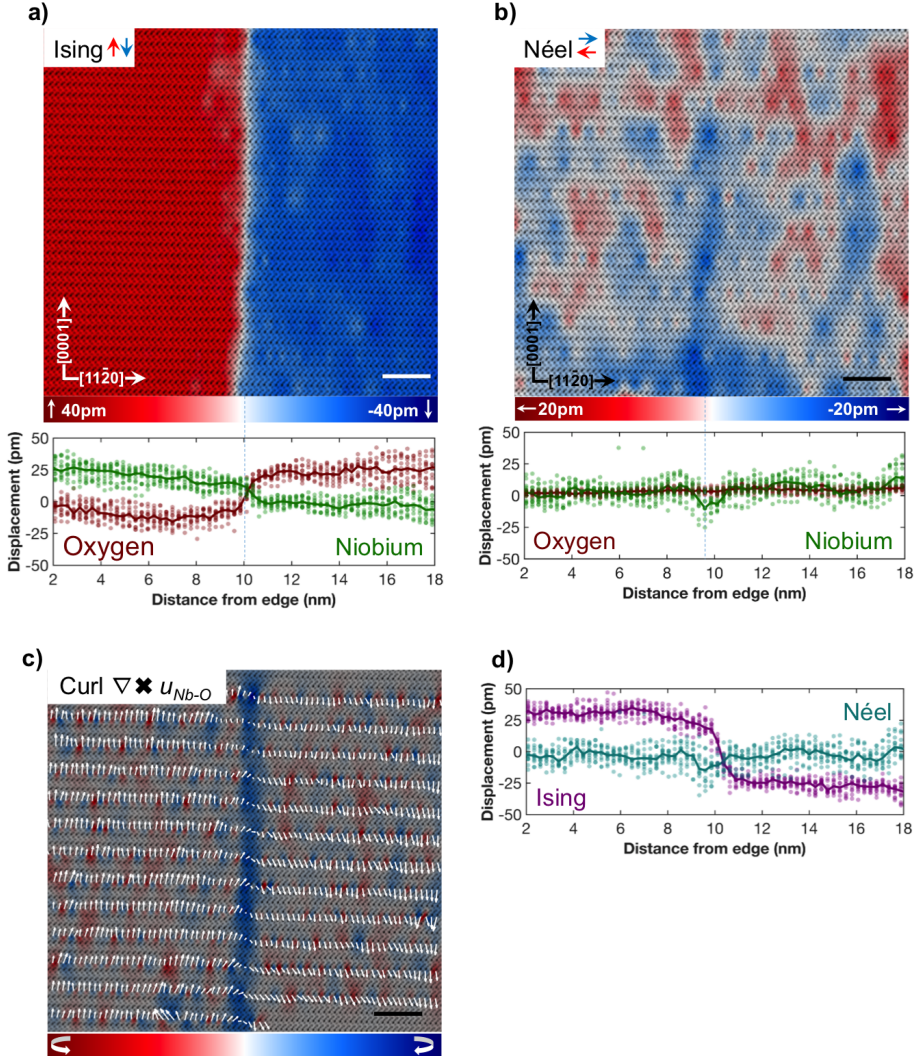


**FIG. 2. Polar displacements measured with BF-STEM.** (a) LiNbO<sub>3</sub> domain wall imaged from [1̄100] zone axis with the polar Ising niobium-oxygen displacements overlaid. Scale bar is 2 nm. The Ising niobium and oxygen along the <0001> direction in green and red respectively with the solid lines referring to the averages are plotted below. (b) Polar niobium-oxygen Néel displacements overlaid on the BF-STEM image. Scale bar is 2 nm. The Néel niobium and oxygen along the <11̄20> direction in green and red respectively with the solid lines referring to the averages are plotted below. (c) Curl of the niobium-oxygen displacement vector overlaid on the BF-STEM image, with the rotation vectors overlaid in white. (d) Niobium and oxygen relative Ising and Néel displacements.

the non-Ising components, we performed DFT calculations of phonons in the high symmetry phase of LiNbO<sub>3</sub>. In agreement with previous calculations we observed three unstable modes at the  $\Gamma$  point - A<sub>2u</sub> and E<sub>u</sub> polar modes with polarization parallel and perpendicular to the [0001] direction respectively and the A<sub>2g</sub> Raman mode (see Table II)[17]. The polar A<sub>2u</sub> mode has a significant overlap with the vector representing the atomic displacements during the phase transition and therefore describes the displacement pattern responsible for the Ising macroscopic polarization of the ground state ferroelectric phase of LiNbO<sub>3</sub>.

Moreover, we observe that the polar displacements along the Néel/Bloch direction (associated with the doubly degenerate E<sub>u</sub> mode), are unstable and the system can thus lower its

energy with polar displacements perpendicular to the [0001] Ising direction. This can explain our experimental results, i.e. the presence of Néel and Bloch polarization directions at the domain wall where the Ising polarization amplitude is strongly reduced along the Ising direction. Besides that, within a bulk ferroelectric domain, the E<sub>u</sub> mode instability is suppressed by the A<sub>2u</sub> mode condensation and the associated strain relaxation, however the energy landscape is still sufficiently shallow to allow deviations of local dipole directions from the Ising <0001> axis. Thus while the A<sub>2u</sub> mode is the dominant mode driving ferroelectricity, the instability from the E<sub>u</sub> modes makes it energetically favorable for the non-Ising fluctuations to arise from the ideal LiNbO<sub>3</sub> polar configuration, thus increasing disorder in the system.

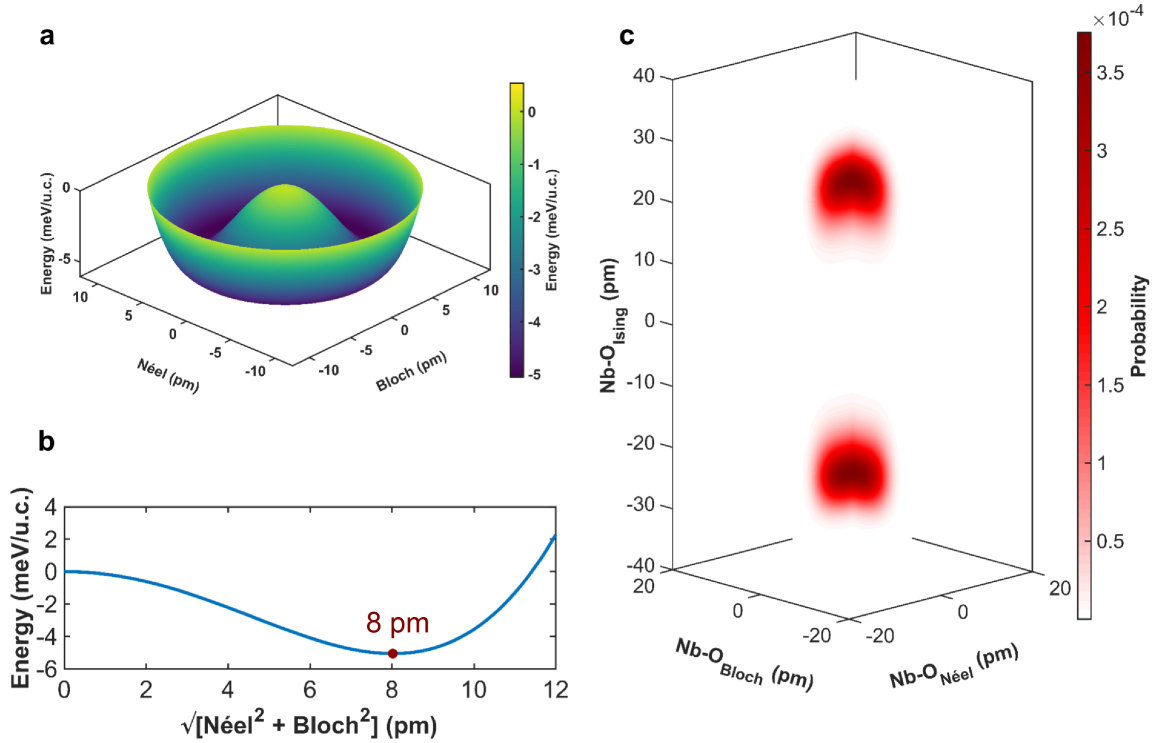


**FIG. 3. First Principles Calculations of displacement configurations.** (a) Goldstone sombrero potential of the relative energy of LiNbO<sub>3</sub> with polar Néel and Bloch displacements associated with the E<sub>u</sub> unstable mode. (b) Energy change as a function of the combined Néel and Bloch displacement magnitude, with energy minima at 8pm. (c) Probability of displacements as a function of the Ising, Néel and Bloch displacements from mean field effective Hamiltonian.

The resultant energy landscape related to the displacements of atoms strictly perpendicular to the  $\langle 0001 \rangle$  Ising axis (E<sub>u</sub> mode) complies with SU(1) unitary group rotation symmetry resulting in the famous Goldstone sombrero potential shape with zero Ising component (Figure 3a). The suppression of the Ising displacements in the  $\langle 0001 \rangle$  direction thus leads to a spontaneous symmetry breakdown giving rise to the perpendicular Néel and Bloch components, with the radial magnitude of the perpendicular components reaching an energy minima at 8pm displacement (Figure 3b). We also note that the experimentally observed Néel magnitudes of approximately 10pm at the domain wall (Figure 2d) are close to the theoretically predicted displacement magnitude at the energy minima. Note however that these experiments cannot quantify the predicted Bloch displacements, because transmission electron microscopy probes a two-dimensional projection of columns of atoms, and Bloch displacements would be parallel to the atomic columns. Thus it was not possible to determine whether the magnitude of the non-Ising polar components stayed constant (massless Goldstone modes) or varied across the domain boundary (massive Higgs modes)[40, 41].

Extending our calculations to the bulk domain, we observe that even in a mono-domain region, the shallow E<sub>u</sub> mode permits fluctuations in the non-Ising polar components. This is shown in Figure 3c where rather than the displacements being clustered at the canonical Ising value, there is a spread in displacement magnitudes in both the Néel and the Bloch

directions. Thus, our theoretical calculations demonstrate that disorder is intrinsic to LiNbO<sub>3</sub> and is not just confined to the domain wall vicinity.

Experimental quantification of these probabilities ( $\rho$ ) of polar displacements along the Ising and Néel displacement orientations in the bulk domain (representative image shown in Figure 4a) is shown in Figure 4b, with the quantification of probability detailed in the section IV F. Even though the displacements do not correspond to one single Ising value and are associated with a spread in Ising and Néel magnitudes, the most probable displacement configuration matches closely with bulk domain values of 20 pm of Ising displacements and  $\approx 0$  pm of Néel displacements. This measured probability distribution is subsequently used to calculate the entropy contribution as a function of the possible Ising and Néel states and compare them with the theoretical predictions. Figure 4c demonstrates the theoretical and experimental contributions to entropy as a function of Ising displacement configurations in brown and blue respectively, with the total probability from the possible Ising configurations being the sum of the contributions of the individual Ising states. Both first principles calculations and experiments demonstrate that intrinsic entropy originating from a spread in displacement configurations is present even in the bulk domain.

This picture is repeated even when measuring the entropy arising as a consequence of a spread of Néel displacement probabilities, as shown in Figure 4d. The integrated entropy

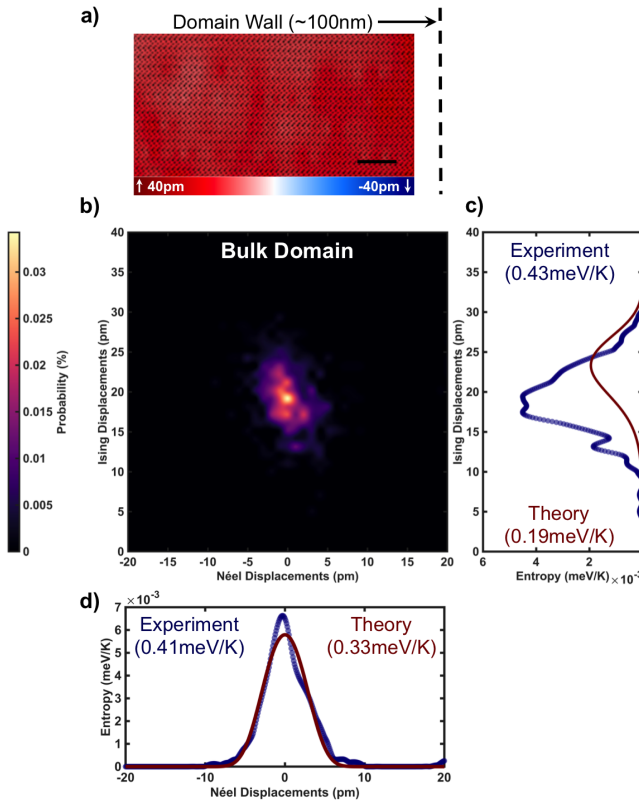


**FIG. 4. Measured probability and polar entropy in the bulk domain in  $\text{LiNbO}_3$ .** (a) Representative STEM image of a bulk domain region approximately 100nm to the left of the domain wall from where the probability distribution and entropy was measured with the Ising displacements overlaid demonstrating a monodomain region. Scale bar is 2nm. (b) Probability distribution of Ising and Néel displacement magnitudes in the bulk domain. (c-d), Theoretically calculated (brown) and experimentally measured (blue) entropy contribution as a function of Ising and Néel displacement orientations in the bulk domain, with the summed contribution in inset.

associated with the Néel component is 0.4meV/K from experiments, while the theory predicts an intrinsic value of 0.33meV/k, which is 82.5% of the experimental value. Thus clearly, the intrinsic entropy contribution dominates the overall Néel entropy in the bulk, and a small fraction ( 17.5%) arises likely from extrinsic effects such as point defects in the congruent composition. The integrated Ising entropy (calculated by integrating the curves in panel Figure 4c as described in section IVF) are 0.43meV/K (experiments) and 0.19 meV/K (theory), indicating a larger contribution to the Ising entropy from the extrinsic defects in the crystal – in other words, the defects appear to create a larger spread in the values of the Ising polarization than in the Néel polarization in a bulk crystal region.

This picture changes significantly in the vicinity of the domain wall (defined here as  $\approx \pm 10\text{nm}$  across the wall – with the STEM image of the representative section shown in Figure 5a), whose probability distribution is plotted in Figure 5b. As expected, we observe a bimodal distribution of the proba-

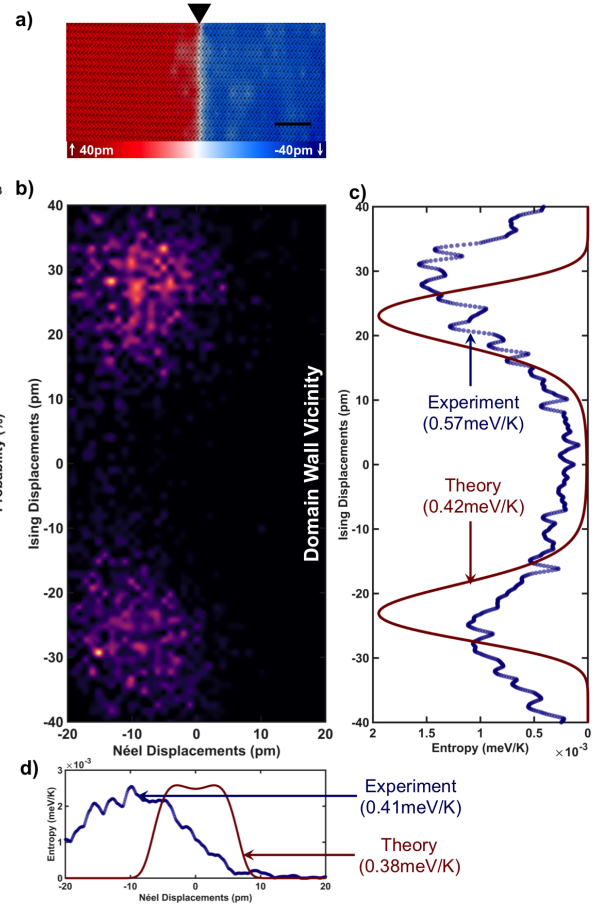


**FIG. 5. Measured probability and polar entropy in the vicinity of the domain wall.** (a) Representative STEM image of a region in the vicinity of the domain wall with Ising displacements overlaid, with the black triangle marker at the top showing the domain wall location. Scale bar is 2nm. (b) Probability distribution of Ising and Néel displacement magnitudes in the vicinity of the domain wall. (c-d) Theoretically calculated (brown) and experimentally measured (blue) entropy contribution as a function of Ising and Néel displacement orientations in the vicinity of the domain wall, with the summed contribution in inset.

ble polar states in the vicinity of the wall, with a significantly more diffuse probability distribution as compared to the probabilities measured in Figure 4b. Both the integrated experimental (0.57meV/K contribution from Néel fluctuations and 0.51meV/K contribution from Ising fluctuations) and theoretical intrinsic entropy (0.38 meV/K of Néel and 0.42 meV/K Ising respectively) contributions shown in Figure 5c and Figure 5d increase in the vicinity of the domain wall as compared to the bulk domain, with the measured entropy in the vicinity of the wall being approximately 25% higher than the bulk domain entropy far away from the wall. It thus indicates that both the intrinsic entropy present from symmetry fluctuations inside the domain and the extrinsic domain wall contribution drive the total entropy at the wall.

This extrinsic increase in entropy can be understood as a consequence of the spread in the Ising displacement mag-

nitudes. As we approach the domain wall, the Ising displacements become progressively smaller, reflected in the BF-STEM measurements ([Figure 2a](#)) and the increased probability of Ising states with zero displacement ([Figure 5c](#)), which are absent in the bulk domain ([Figure 4c](#)). The  $E_u$  mode instability, which was suppressed in the bulk domain, now leads to a spontaneous symmetry breakdown, leading to an increase in the possible Néel states ([Figure 5d](#)). It is also instructive to note that the Néel displacement probability assumes its maxima at approximately 10pm, extremely close to the energy minima at 8pm predicted by simulations ([Figure 3b](#)). It is this spontaneous symmetry breaking that is thus driving the Néel displacement at the domain wall.

The observation of non-Ising displacements at the domain wall, can have a significant contribution to the electrostatic potential energy [[15, 16, 31, 42–44](#)]. To further understand the contribution of the electrostatic potential energy in the system, we experimentally quantified the charge accumulation at both the bulk domain and in the vicinity of the domain wall (detailed in [section IV G](#)). The electrostatic potential energy contribution in the vicinity of the domain wall was measured to be approximately 0.45meV, and approximately 0.37meV in the bulk domain. The thermodynamic free energy, given by the famous Gibbs's relationship ( $\Delta G = \Delta H - T\Delta S$ ), where  $T$  is the temperature,  $S$  is the entropy,  $H$  is the enthalpy and  $G$  is the free energy, determines the stability of a closed system. Using the experimentally calculated entropy values from [Figure 4c](#) and [Figure 4d](#), the  $-T\Delta S$  at 300 K is -152meV at the bulk domain. The  $-T\Delta S$  decreases further to -298meV at 300K for the domain wall ([Figure 5c](#) and [Figure 5d](#)). Thus, while electrostatic energy increases in the system, the total free energy decreases as a result of increased entropy, demonstrating it is entropy rather than electrostatics, which dominates the non-Ising polarization rotations in  $\text{LiNbO}_3$ .

While experimental observations cannot capture the Bloch contribution to the entropy, it is interesting to note the similarity in magnitude of the theoretically predicted and experimentally measured entropy contributions. In fact, experimental measurements should be higher due to temperature fluctuations and point defects, vacancies, and interstitials that cannot be effectively captured in a first principles model. In spite of such deviations from the ideal structure, theoretical predictions consistently predict higher entropy at the domain walls and the entropy values of 75-80% of the measured experimental entropy, indicating that the observed polar disorder is predominantly intrinsic to  $\text{LiNbO}_3$ .

#### IV. CONCLUSIONS

Our results presented here are the first known experimental quantification of absolute configurational entropy from atomic resolution position metrology. The advent of aberration correction has now enabled the quantitative picometer precision imaging and metrtology of atom positions - which allows the direct visualization of disorder in a system. While configurational entropy has shown to be driving the properties of ferroelectrics, this is the first direct measurement in a

system [[45, 46](#)].

Based on our results, an intriguing picture of a classic, nominally Ising ferroelectric emerges from our experimental STEM imaging and theoretical DFT calculations. At the domain walls, we observe non-Ising Néel displacements that are thermodynamically stabilized from the corresponding increase in entropy. Non-Ising displacements and fluctuations occur throughout the bulk domain and the domain walls due to the intrinsic polar entropy. The magnitude of this polar entropy is increased at the domain wall according to both the theoretical and experimental calculations.

Our study reveals a classical single crystal Ising ferroelectric, hiding considerable local intrinsic entropy that is present even in the bulk domain. This is despite  $\text{LiNbO}_3$  having only a single symmetry allowed net polarization direction, large coercive fields for domain reversal, and a high Curie temperature indicating its stability at room temperature [[18, 38, 47, 48](#)]. This entropy is enabled by the shallow  $E_u$  mode thermodynamic landscape, where the polar fluctuations are stabilized by the increase in disorder. At the domain wall, however, the presence of symmetry breaking from the wall itself leads to an increase in the entropy. Along with that, as the Ising displacement gets suppressed in the vicinity of the wall, the  $E_u$  mode instability dominates leading to energetically favorable Néel and Bloch displacements.

Our results also hint at a probable reason why entropy calculations in ferroelectrics remain so scarce in the literature – a 0K calculation of a ferroelectric will obviously not capture polar fluctuations, and will instead converge to the energetic ground state - which is the classical Ising formulation. In fact, these polar fluctuations increase the electrostatic potential energy, and thus it is tempting to dismiss them as unstable, or consider their occurrence only through the presence of strain or dopants. However, this picture ignores the energy stabilization afforded by entropy which compensates the energy increase from electrostatics at room temperature. We rather show that this disorder is intrinsic to ferroelectrics and can exist even in the absence of any extrinsic factors.

Thus, these results challenge the rigid classification of ferroelectrics into ideal and relaxor ferroelectrics [[49–54](#)]. Polar disorder is a highly sought after component for functional systems like piezoelectrics and electrocalorics, and our study reveals a novel pathway towards engineering such disorder by relying on the thermodynamic stability afforded by increasing entropy [[55–60](#)]. The electron microscopy based metrolology techniques developed here thus allow for similar studies to be performed in other systems, even beyond ferroelectrics - allowing the electron microscope to be used not only as an imaging system, but also for atomic resolution thermodynamic quantification.

#### ACKNOWLEDGEMENTS

D.M., L.M., V.G. and N.A. would like to acknowledge support from the Penn State Center for Nanoscale Sciences, an NSF MRSEC, funded under the grant number DMR-1420620. S. P. and E.B. acknowledge the supported provided by the

University of Liège and the EU in the context of the FP7-PEOPLE-COFUND-BeIPD project, the ARC project AIMED, and the DARPA Grant No. HR0011727183-D18AP00010 (TEE Program) and the Céci facilities funded by F.R.S-FNRS (Grant No. 2.5020.1) and Tier-1 supercomputer of the Fédération Wallonie-Bruxelles funded by the Walloon Region (Grant No. 1117545). D.M., V.G. and N.A. would like to acknowledge the Penn State Materials Characterization Laboratory for use of their sample preparation and electron microscopy facilities. D.M. would like to acknowledge Dr. Haiying Wang of Penn State Materials Characterization Laboratory for help with sample preparation.

## AUTHOR CONTRIBUTIONS

D.M., V.G. and N.A. designed the project. D.M. prepared the electron microscopy samples, and acquired the transmission electron microscopy data, assisted by K.W. D.M. developed the MATLAB subroutines for analysis. D.M., assisted by L.M., and advised by N.A. and V.G. analyzed the electron microscopy data. S.P., assisted by E.B. performed the first principles calculations. D.M., advised by N.A. and V.G. wrote the manuscript. All authors discussed the results and commented on the manuscript.

## COMPETING INTERESTS

The authors declare no competing financial interests.

## APPENDIX

### A. Imaging and preparation of $\text{LiNbO}_3$ samples

We obtained commercially available periodically poled single crystal congruent  $\text{LiNbO}_3$  crystals with  $6.7\mu\text{m}$  domain repetition from Deltronic Industries. The electron transparent samples were prepared by focused ion beam (FIB) using a FEI Helios G2 system with a 30keV gallium ion beam used for sample liftâšout with the domain walls lying edge on. Final polishing was performed with 0.5kV ion beams till the sample became electron transparent at an accelerating of 2kV to ensure that the sample was thin enough for imaging oxygen atoms[61]. Following the preparation of electron transparent samples, we first imaged the  $\text{LiNbO}_3$  foil with conventional TEM (CTEM) mode (see Figure 6a), with the obtained diffraction pattern demonstrating that the sample is being observed from the zone of interest - the  $\langle 1\bar{1}00 \rangle$  (see Figure 6b). The samples were imaged in the CTEM mode with a slight defocus ( $\approx 5\text{nm}$ ) for help in locating the domain walls through diffraction contrast.

Following the identification of the domain walls, we subsequently used STEM imaging in a FEI Titan<sup>3</sup> aberration corrected transmission electron microscope (TEM) corrected for upto third order spherical aberrations. Annular dark Field Scanning TEM (ADF-STEM) imaging was performed using

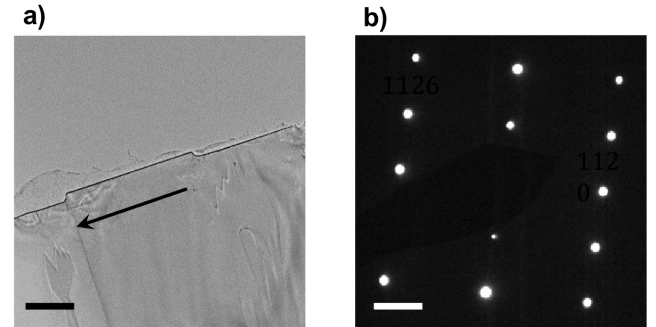


**FIG. 6. Low magnification TEM image and electron diffraction pattern.** (a) Low magnification CTEM with the domain wall (marked by the arrow) visible due to diffraction contrast at the wall. (b) Diffraction pattern from the image in Figure 6a confirming the  $[1\bar{1}00]$  zone axis.

Fischione detectors at a camera length of 145mm with an inner collection semi-angle of 32mrad, and an outer collection semi-angle of 188 mrad. Bright Field Scanning TEM (BF-STEM) images were simultaneously collected with Gatan detectors with an outer collection semi-angle of 15mrad. Simultaneous BF-STEM and ADF-STEM imaging was performed with fast scan directions oriented at  $-5^\circ$  and  $85^\circ$  with respect to the domain wall. The two image sets were combined and subsequently corrected post acquisition for scan drift using a previously developed procedure[62]. Based on MacTempasX simulations, tilt was not a contributing error to the  $\text{LiNbO}_3$  polarization calculations (see Figure 17).

### B. Displacements in the Bulk Domain

Three different regions (Figure 7, Figure 8, Figure 9) are shown as different regions of the bulk domain that were imaged. While all three are mono-domain regions, it is instructive to note that the Ising displacement itself is not entirely constant even 100nm into the domain, with the displacement demonstrating magnitude variations as seen in Figure 7a and Figure 8a. Both these regions are additionally associated with regions of Néel displacements as can be observed in Figure 7b and Figure 8b. These Néel displacements are ultimately visible in the rotation maps (see Figure 7c and Figure 8c), demonstrating polar non-Ising components arising even in bulk domain regions approximately 100nm away from the domain wall. This variation in polar components is ultimately reflected in increased entropy.

Figure 9 demonstrates a section of the bulk domain, approximately 20nm away from the domain wall. As could be observed in this section, the total Ising displacements are significantly smaller than expected, with a corresponding decrease in Néel displacements, demonstrating regions of decreased polarity embedded in the domain near the domain wall.

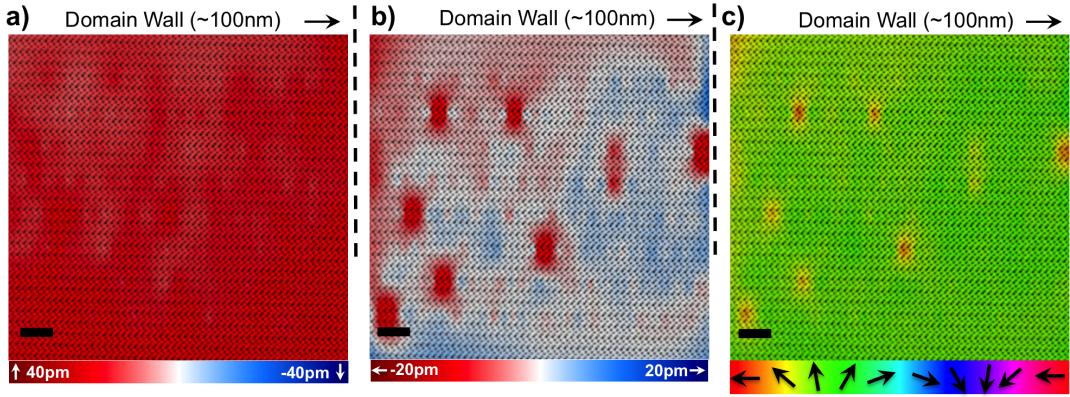


**FIG. 7. Bulk domain HR-STEM image with the polarization and rotation map overlaid on top at a location  $\approx 100\text{nm}$  away from wall.** (a) Ising displacement mapped out over the bulk domain. (b) Néel displacement map showing regions of no Néel displacements, and nanoregions of high Néel displacements. (c) Rotation colormap. Scale bar in all images is 2nm.

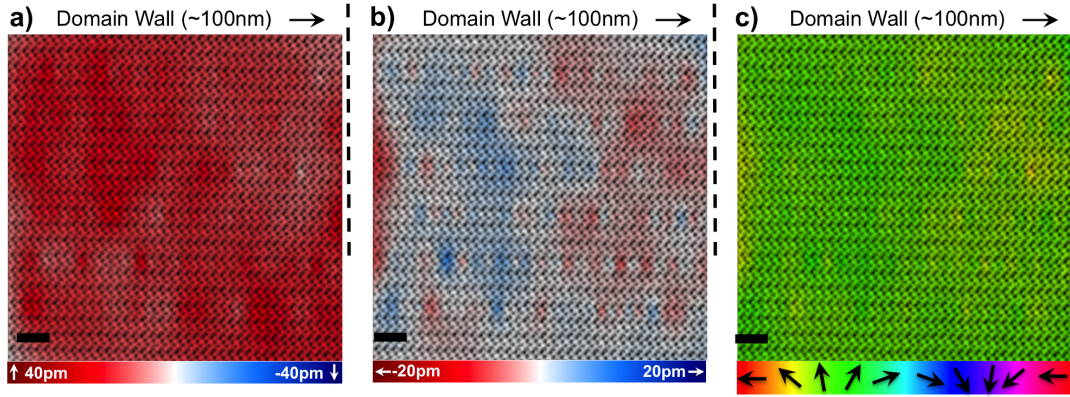


**FIG. 8. Bulk domain imaging  $\approx 100\text{nm}$  away from wall.** (a) Ising displacement mapped out over the bulk domain. (b) Néel displacement map showing regions of lower Néel displacements. (c) Rotation colormap. Scale bar in all images is 2nm.

### C. Displacements in the vicinity of the Domain Wall

Four other domain wall regions (labeled as regions 2-5, with region imaged in Figure 2) were also characterized in the electron microscope, as demonstrated in Figure 10, Figure 11, Figure 12 and Figure 13. As could be observed from all the systems the domain wall is consistently associated with significant Néel type non-Ising distortions. One of the regions of the domain wall, Figure 10 also demonstrates Néel distortions in both positive and negative directions, with leftward Néel distortions precipitating primarily at the domain wall. Also, the thickness of the Ising component at the domain wall is not uniform at different regions of the domain wall, with Figure 11 demonstrating significantly wider walls compared to the other regions imaged.

### D. First principles calculations

First principles calculations were done using the density functional theory approximation as implemented in the ABINIT software package (v.8.4.3)[63–66]. We chose the

libxc implementation of PBEsol GGA functional to describe the exchange-correlation energy contribution, and the valence electrons were treated through norm-conserving pseudopotentials obtained through the PseudoDojo project[67–71]. The planewave kinetic cut-off energy was taken to be equal to 50 Ha and the Brillouin zone was sampled using a  $6 \times 6 \times 6$  Monkhorst-Pack mesh of special  $k$  points[72]. To determine the structure of the paraelectric R $\bar{3}$ c phase structure of LiNbO<sub>3</sub>, we considered a primitive 10 atom unit cell and performed a relaxation of atomic positions followed by an energy optimization with respect to changes both in lattice vectors and the reduced atomic coordinates under an imposed constraint of the fixed R $\bar{3}$ c space-group symmetry, with the primitive unit cell dimensions given in Table I. The high-accuracy structural relaxation was performed until the calculated force magnitudes were less than  $10^{-8}\text{ev\AA}$ , and the absolute values of stress tensor components do not exceed  $10^{-7}\text{GPa}$ . We performed density functional perturbation theory calculations (DFPT) so as to identify the unstable phonon modes (Table II)[73].

To construct the minimal effective Hamiltonian model we have first computed the internal energy landscapes for all

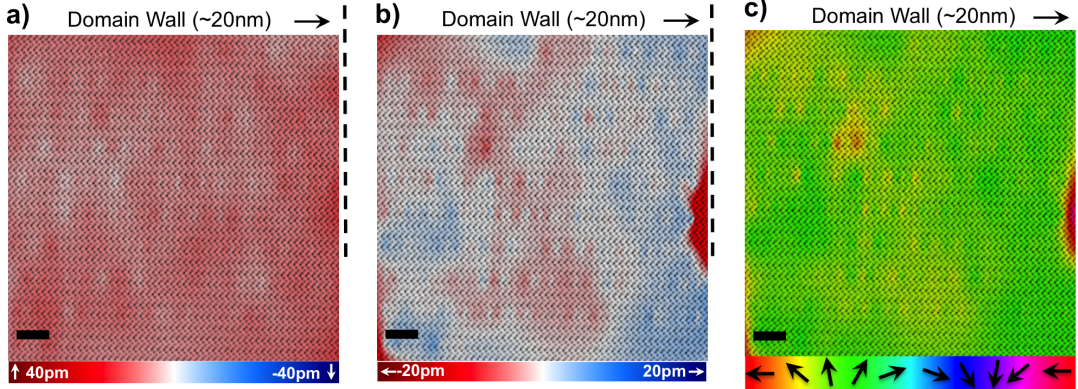


**FIG. 9. Bulk domain  $\approx 20\text{nm}$  away from wall.** (a) Ising displacement mapped out over the bulk domain, showing significantly lower displacements in comparison to other imaged regions. (b) Néel displacement map showing regions of lower Néel displacements. (c) Rotation color map. Scale bar in all images is 2nm

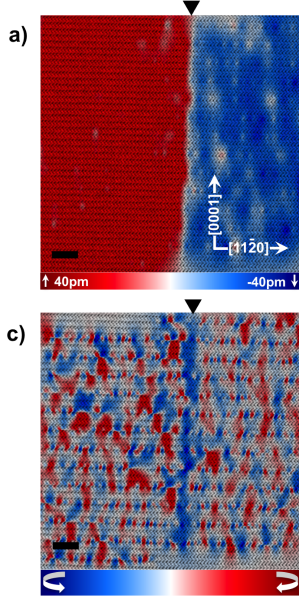


**FIG. 10. Domain wall in Region 2.** (a) Ising displacements at region 2 of the domain wall with non-equivalent polarization on either sides. (b) Néel displacements demonstrating the presence of strong alternating Néel components. (c) Curl of the polar niobium-oxygen displacement map with slight decrease at the domain wall. (d) Rotation map of the polar niobium-oxygen displacements. Scale bar in all images is 2nm.

identified unstable modes. For this, we have performed DFT calculations of the total energy change upon gradually condensing the unstable modes into the structure. The resulting curves were fitted with the 8<sup>th</sup> order polynomials as given by Equation 1.

$$E_M = \kappa_M x^2 + \alpha_M x^4 + \gamma_M x^6 + \delta_M x^8 \quad (1)$$

where  $x$  denotes the amplitude of the mode  $M$ . Similarly, performing calculations of energy changes induced by displace-

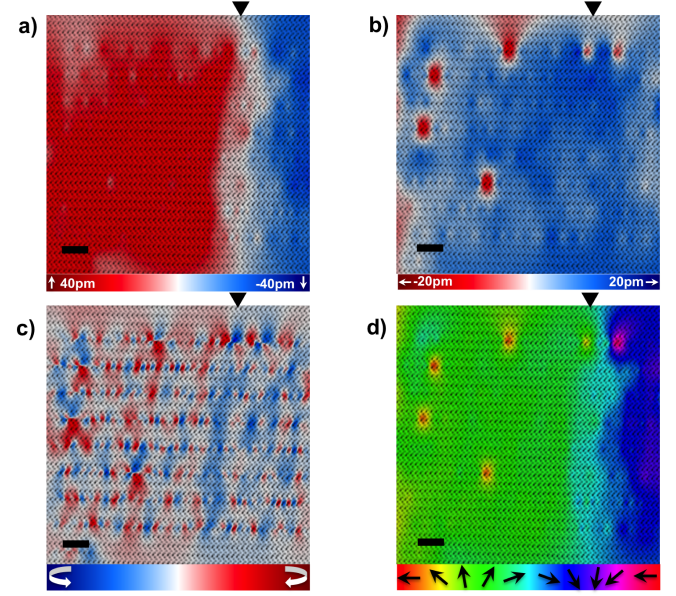


**FIG. 11. Domain wall in Region 3.** (a) Ising displacements at region 3 of the domain wall with non-equivalent polarization on either sides. (b) Néel displacements demonstrating the presence of consistent and uniform Néel components in contrast to region 2 (Figure 10). (c) Curl of the polar niobium-oxygen displacement map with a small discernible change at the domain wall. (d) Rotation map of the polar niobium-oxygen displacements. Scale bar in all images is 2nm.

ments involving not a single but two phonon modes allows to reconstruct the effective mode interactions that we take here to be of the form

$$E_{int}^{M_1 M_2} = g M_1 M_2 x^2 y^2 \quad (2)$$

where  $x$  and  $y$  denote the amplitudes of the  $M_1$  and  $M_2$  modes. The interaction of local modes with strain is taken into account by fitting the dependences of elastic stresses on the mode amplitudes. Finally, the elastic energy produced by the deformations of the cell shape and volume is taken into account in the harmonic approximation. The elastic constants

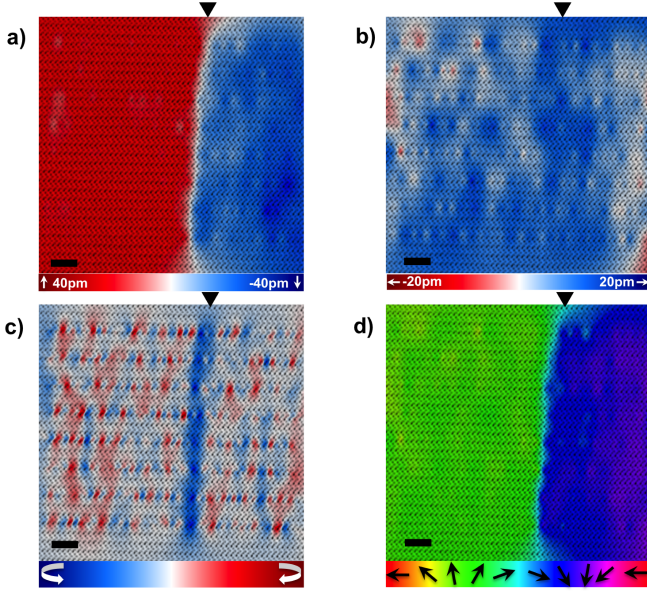


**FIG. 12. Domain wall in Region 4.** (a) Ising displacements at region 4 of the domain wall with non-equivalent polarization on either sides. (b) Néel displacements demonstrating the presence Néel regions, not limited to only the domain wall. (c) Curl of the polar niobium-oxygen displacement map with a significant change only at the domain wall. (d) Rotation map of the polar niobium-oxygen displacements. Scale bar in all images is 2nm.

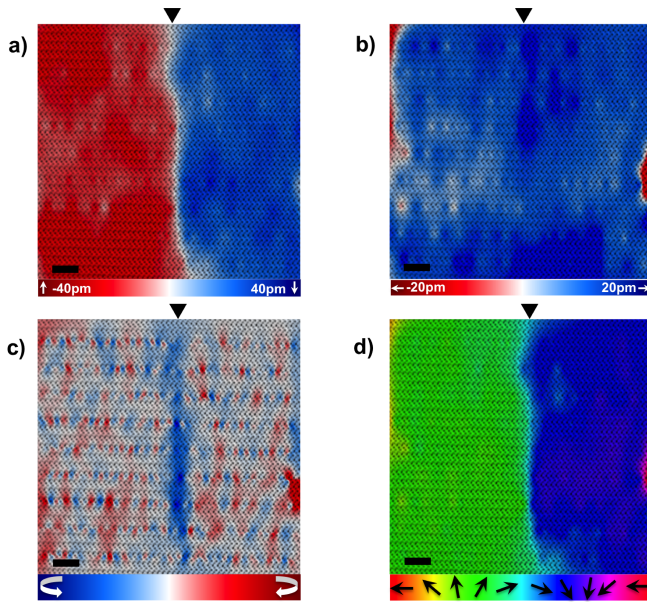


**FIG. 13. Domain wall in Region 5.** (a) Ising displacements at region 5 of the domain wall with a kink in the wall. (b) Quasi uniform Néel displacements in the vicinity of the domain wall. (c) Curl of the polar niobium-oxygen displacement map. (d) Rotation map of the polar niobium-oxygen displacements, with the Ising kink being visible. Scale bar in all images is 2nm.

Atom Position	
Li1	(0, 0, 1/2)
Nb1	(0, 0, 0)
O1	(-1/3, -1/3 + x, 7/12)
O2	(1/3 - x, -x, 7/12)
O3	(x, 1/3, 7/12)

**TABLE I.** Calculated hexagonal co-ordinates of atoms of the primitive unit cell of paraelectric  $\text{LiNbO}_3$ . The lattice parameters are  $a = 518\text{pm}$  and  $c = 1364.6\text{pm}$ .

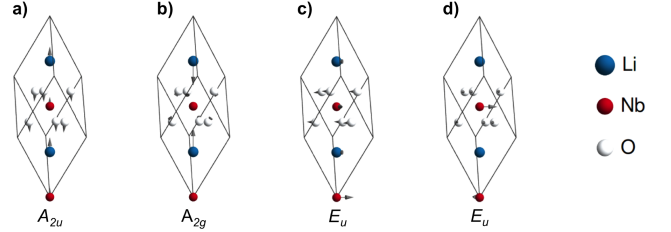


**FIG. 14.** Eigenvectors of (a) the  $A_{2u}$  mode (b) the  $A_{2g}$  mode and (c,d) the two eigenvectors corresponding to the degenerate  $E_u$  mode aligned with x and y Cartesian axis respectively.

are computed from density functional perturbation theory. Note that in the case of the  $E_u$  mode, all the energy expansion coefficients are assumed to depend on the displacement direction in the (0001) plane, however the calculations show that such in-plane anisotropy can be safely neglected. In the described model, the short-range and long-range dipolar interactions between different modes are taken into account in the mean-field approximation. These energetic contributions essentially lead to renormalization of the  $\kappa_M$  and  $f_{M_1 M_2}$  coefficients. To determine the most important low-energy atomic displacements patterns we further performed the density functional perturbation theory calculations so as to identify low frequency phonon modes for the obtained ground state, with the obtained calculations in Table II.

### E. Calculation of polar modes

The calculated polar modes for the paraelectric  $\text{LiNbO}_3$  unit cell (Table I) are shown in Table II. As could be observed, there are four polar modes, with the  $A_{2u}$  mode driving ferroelectricity, while it is the degenerate  $E_u$  modes that drive the non-Ising Néel and Bloch displacements. The polar phonon mode displacements are visualized in Figure 14, which plot the individual atom displacements corresponding to the polar modes.

### F. Metrology of polar entropy from BF-STEM images

Entropy measurements are performed using three sets of STEM data



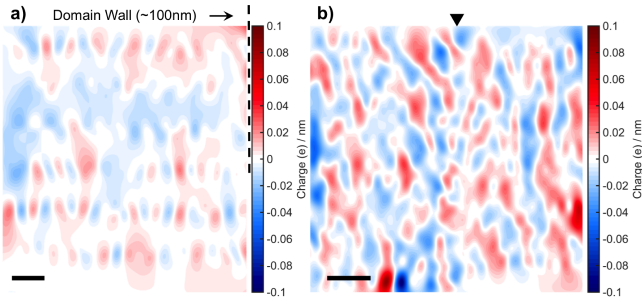


**FIG. 15. Calculated charge accumulation.** (a) Charge accumulation at a region of the bulk domain ( $\approx 100\text{nm}$ ) away from the wall. The polarization maps are given in [Figure 7a](#) and [Figure 7b](#) for the Ising and Néel displacements respectively. (b) Charge accumulation in the vicinity of the domain wall (Region 1), with the black triangle showing the domain wall location. The polarization maps are given in [Figure 2a](#) and [Figure 2b](#) for the Ising and Néel displacements respectively. Scale bar in both images is 2nm.

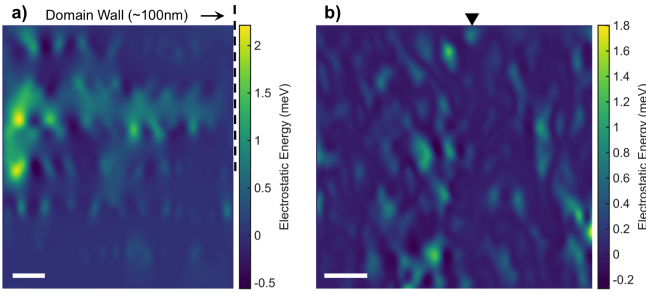


**FIG. 16. Measured electrostatic potential energy.** (a) Potential energy at a region of the bulk domain ( $\approx 100\text{nm}$ ) away from the wall. The polarization maps are given in [Figure 7a](#) and [Figure 7b](#) for the Ising and Néel displacements respectively. (b) Potential energy in the vicinity of the domain wall (Region 1), with the domain wall location shown by the black triangle. The polarization maps are given in [Figure 2a](#) and [Figure 2b](#) for the Ising and Néel displacements respectively. Scale bar in both images is 2nm. Potential energy was calculated with  $\epsilon_r = 4.821$ [\[74\]](#).

#### G. Calculation of charge accumulation and electrostatic potential energy

Charge calculations were performed by first estimating the Born effective charge tensors theoretically, with the calculated Born effective charges presented in [Table III](#). The calculated polar displacements from a representative bulk domain region ([Figure 7](#)) and a representative domain wall region ([Figure 2](#)) respectively are vector multiplied with the Born effective charge tensors ([Table III](#)) for the niobium and oxygen atoms only, since we cannot image the lithium atoms. The divergence of this polarization is now the charge accumulation, which is presented in [Figure 15](#), with [Figure 15a](#) showing the charge accumulation in the bulk domain region, and [Figure 15b](#) demonstrating the charge accumulation in the domain wall vicinity.

Thus, for each image, we have a total charge distribution. Assuming that each pixel corresponds to a charge value, then

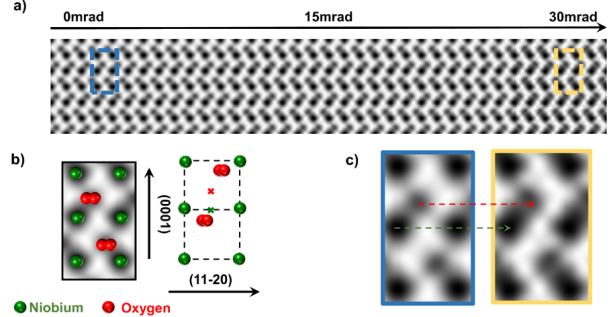


**FIG. 17. Evolution of BF-STEM image as a function of  $\alpha$  tilt.** (a) Multislice simulations of BF-STEM image of  $\text{LiNbO}_3$  using the conditions detailed in [Table IV](#) without aberrations as a function of  $\alpha$  tilt from 0 mrad (no tilt) to 30 mrad of  $\alpha$  tilt. (b) Zoomed in section with the niobium atoms in green and the oxygen atoms in red overlaid on top. (c) Comparison of the tilt effects at 0 mrad and 30 mrad showing how the oxygen atom moves up (red arrow) and the niobium atom no longer maintains a circular shape (green arrow).

the total number of pixels ( $N$ ) refers to the total possible charge values. The electrostatic potential energy is then calculated using [Equation 9](#), obtained through an integration of Coulomb's law

$$U_E = \frac{1}{2} \sum_{x=1}^N q_x \sum_{y=1}^{N(y \neq x)} \left( \frac{1}{4\pi\epsilon_0\epsilon_{\text{LiNbO}_3}} \times \frac{q_y}{r_{xy}} \right) \quad (9)$$

where  $q_x$  refers to the charge at a certain pixel, and  $r_{xy}$  refers to the distance between distance between the  $x^{\text{th}}$  and the  $y^{\text{th}}$  pixel. The term  $1/2$  prevents double counting the potential energy contribution between  $x$  and  $y$ , and  $y$  and  $x$  positions. The  $\epsilon_{\text{LiNbO}_3}$  is 4.821[\[74\]](#). The calculated electrostatic potential energy for the two regions are shown in [Figure 16a](#) for the domain, and [Figure 16b](#) for the domain wall.

#### H. Simulation of $\text{LiNbO}_3$ BF-STEM images

BF-STEM simulations of the  $\text{LiNbO}_3$  crystal structure were performed using the MacTempasX commercial software to understand the effect of tilt on imaging and atom position metrology, with the simulation parameters being enumerated in [Table IV](#), with the effect of increasing  $\alpha$  tilt being shown in [Figure 17](#)[\[75\]](#). As could be observed, the relative distance being the niobium-oxygen columns in sensitive to tilt, with the distance decreasing with increasing tilt. However, since the average Niobium-Oxygen polar Ising displacements match extraordinarily closely with the theoretical values in the domain wall figures presented in this work, tilt is not a contributing factor. Additionally, while increasing tilt would result in closer niobium-oxygen columns in the up domain, as shown in [Figure 17c](#), it will also thus result in an increased distance in the down domain. However, the symmetric displacements observed ([Figure 2](#), [Figure 10](#),[Figure 11](#),[Figure 11](#),[Figure 12](#),[Figure 13](#)) would indicate



- press, 1977.
- [11] Karin M Rabe, Charles H Ahn, and Jean-Marc Triscone. *Physics of ferroelectrics: a modern perspective*, volume 105. Springer Science & Business Media, 2007.
- [12] Nicola A Spaldin. A beginner's guide to the modern theory of polarization. *Journal of Solid State Chemistry*, 195:2–10, 2012.
- [13] Alexander Kirillovich Tagantsev, L Eric Cross, and Jan Fousek. *Domains in ferroic crystals and thin films*. Springer, 2010.
- [14] Gustau Catalan, J Seidel, R Ramesh, and James F Scott. Domain wall nanoelectronics. *Reviews of Modern Physics*, 84(1):119, 2012.
- [15] EA Eliseev, AN Morozovska, GS Svechnikov, Venkatraman Gopalan, and V Ya Shur. Static conductivity of charged domain walls in uniaxial ferroelectric semiconductors. *Physical Review B*, 83(23):235313, 2011.
- [16] Tomas Sluka, Alexander K Tagantsev, Petr Bednyakov, and Nava Setter. Free-electron gas at charged domain walls in insulating BaTiO<sub>3</sub>. *Nature communications*, 4:1808, 2013.
- [17] M Veithen and Ph Ghosez. First-principles study of the dielectric and dynamical properties of lithium niobate. *Physical Review B*, 65(21):214302, 2002.
- [18] David A Scrymgeour, Venkatraman Gopalan, Amit Itagi, Avadh Saxena, and Pieter J Swart. Phenomenological theory of a single domain wall in uniaxial trigonal ferroelectrics: Lithium niobate and lithium tantalate. *Physical Review B*, 71(18):184110, 2005.
- [19] Venkatraman Gopalan, Terence E Mitchell, and Kurt E Sicakfus. Switching kinetics of 180° domains in congruent LiNbO<sub>3</sub> and LiTaO<sub>3</sub> crystals. *Solid state communications*, 109(2):111–117, 1998.
- [20] Helen D Megaw. A note on the structure of lithium niobate, LiNbO<sub>3</sub>. *Acta Crystallographica Section A: Crystal Physics, Diffraction, Theoretical and General Crystallography*, 24(6):583–588, 1968.
- [21] Donghua Lee, Rakesh K Behera, Pingping Wu, Haixuan Xu, YL Li, Susan B Sinnott, Simon R Phillipot, LQ Chen, Venkatraman Gopalan, et al. Mixed Bloch-Neel-Ising character of 180° ferroelectric domain walls. *Physical Review B*, 80(6):060102, 2009.
- [22] YJ Wang, D Chen, YL Tang, YL Zhu, and XL Ma. Origin of the Bloch-type polarization components at the 180° domain walls in ferroelectric PbTiO<sub>3</sub>. *Journal of Applied Physics*, 116(22):224105, 2014.
- [23] Xian-Kui Wei, Chun-Lin Jia, Tomas Sluka, Bi-Xia Wang, Zuo-Guang Ye, and Nava Setter. Néel-like domain walls in ferroelectric Pb(Zr, Ti)O<sub>3</sub> single crystals. *Nature communications*, 7:12385, 2016.
- [24] Jacek C Wojdel and Jorge Iniguez. Ferroelectric transitions at ferroelectric domain walls found from first principles. *Physical review letters*, 112(24):247603, 2014.
- [25] Venkatraman Gopalan, Terence E Mitchell, and Kurt E Sicakfus. Switching kinetics of 180° domains in congruent LiNbO<sub>3</sub> and LiTaO<sub>3</sub> crystals. *Solid state communications*, 109(2):111–117, 1998.
- [26] Yasunori Furukawa, Masayoshi Sato, Kenji Kitamura, and Fumio Nitanda. Growth and characterization of off-congruent LiNbO<sub>3</sub> single crystals grown by the double crucible method. *Journal of crystal growth*, 128(1-4):909–914, 1993.
- [27] Venkatraman Gopalan, QX Jia, and TE Mitchell. In situ video observation of 180° domain kinetics in congruent LiNbO<sub>3</sub> crystals. *Applied physics letters*, 75(16):2482–2484, 1999.
- [28] Sungwon Kim, Venkatraman Gopalan, and B Steiner. Direct x-ray synchrotron imaging of strains at 180° domain walls in congruent LiNbO<sub>3</sub> and LiTaO<sub>3</sub> crystals. *Applied Physics Letters*, 77(13):2051–2053, 2000.
- [29] S Grilli, M Paturzo, L Miccio, and P Ferraro. In situ investigation of periodic poling in congruent LiNbO<sub>3</sub> by quantitative interference microscopy. *Measurement Science and Technology*, 19(7):074008, 2008.
- [30] Greg Stone, Colin Ophus, Turan Birol, Jim Ciston, Che-Hui Lee, Ke Wang, Craig J Fennie, Darrell G Schlom, Nasim Alem, and Venkatraman Gopalan. Atomic scale imaging of competing polar states in a Ruddlesden-Popper layered oxide. *Nature communications*, 7:12572, 2016.
- [31] Takao Matsumoto, Ryo Ishikawa, Tetsuya Tohei, Hideo Kimura, Qiwen Yao, Hongyang Zhao, Xiaolin Wang, Dapeng Chen, Zhenxiang Cheng, Naoya Shibata, et al. Multivariate statistical characterization of charged and uncharged domain walls in multiferroic hexagonal YMnO<sub>3</sub> single crystal visualized by a spherical aberration-corrected stem. *Nano letters*, 13(10):4594–4601, 2013.
- [32] Young-Min Kim, Stephen J Pennycook, and Albina Y Borisevich. Quantitative comparison of bright field and annular bright field imaging modes for characterization of oxygen octahedral tilts. *Ultramicroscopy*, 181:1–7, 2017.
- [33] Qian He, Ryo Ishikawa, Andrew R Lupini, Liang Qiao, Eun J Moon, Oleg Ovchinnikov, Steven J May, Michael D Biegalski, and Albina Y Borisevich. Towards 3D mapping of BO<sub>6</sub> octahedron rotations at perovskite heterointerfaces, unit cell by unit cell. *ACS Nano*, 9(8):8412–8419, 2015.
- [34] Debangshu Mukherjee, Leixin Miao, Greg Stone, and Nasim Alem. MPFit: A robust method for fitting atomic resolution images with multiple gaussian peaks. Manuscript submitted for publication, 2018.
- [35] SC Abrahams, J Mi Reddy, and JL Bernstein. Ferroelectric lithium niobate. 3. single crystal x-ray diffraction study at 24°C. *Journal of Physics and Chemistry of Solids*, 27(6-7):997–1012, 1966.
- [36] H Boysen and F Altendorfer. A neutron powder investigation of the high-temperature structure and phase transition in LiNbO<sub>3</sub>. *Acta Crystallographica Section B: Structural Science*, 50(4):405–414, 1994.
- [37] Julie Gonnissen, Dmitry Batuk, Guillaume F Nataf, Lewys Jones, Artem M Abakumov, Sandra Van Aert, Dominique Schryvers, and Ekhard KH Salje. Direct observation of ferroelectric domain walls in LiNbO<sub>3</sub>: Wall-meanders, kinks, and local electric charges. *Advanced Functional Materials*, 26(42):7599–7604, 2016.
- [38] GA Smolenskii, NN Krainik, NP Khuchua, VV Zhdanova, and IE Mylnikova. The curie temperature of LiNbO<sub>3</sub>. *physica status solidi (b)*, 13(2):309–314, 1966.
- [39] Salia Cherifi-Hertel, Hervé Bulou, Riccardo Hertel, Grégory Taupier, Kokou Dodzi Honorat Dorkenoo, Christian Andreas, Jill Guyonnet, Iaroslav Gaponenko, Katia Gallo, and Patrycja Paruch. Non-ising and chiral ferroelectric domain walls revealed by nonlinear optical microscopy. *Nature communications*, 8:15768, 2017.
- [40] Jeffrey Goldstone. Field theories with «superconductor» solutions. *Il Nuovo Cimento (1955-1965)*, 19(1):154–164, 1961.
- [41] Peter W Higgs. Broken symmetries and the masses of gauge bosons. *Physical Review Letters*, 13(16):508, 1964.
- [42] V Ya Shur, EL Rumyantsev, EV Nikolaeva, and EI Shishkin. Formation and evolution of charged domain walls in congruent lithium niobate. *Applied physics letters*, 77(22):3636–3638, 2000.
- [43] Thomas Kämpfe. *Charged Domain Walls in Ferroelectric Single Crystals*. PhD thesis, Technische Universität Dresden, 11 2016.
- [44] Christian Godau, Thomas Kämpfe, Andreas Thiessen, Lukas M Eng, and Alexander Haußmann. Enhancing the domain wall conductivity in lithium niobate single crystals. *ACS nano*, 11(5):4816–4824, 2017.

- [45] Alessio Filippetti, Pietro Delugas, Maria Ilenia Saba, and Alessandro Mattoni. Entropy-suppressed ferroelectricity in hybrid lead-iodide perovskites. *The Journal of Physical Chemistry Letters*, 6(24):4909–4915, 2015.
- [46] Wenjuan Wei, Wei Li, Keith T Butler, Guoqiang Feng, Christopher J Howard, Michael A Carpenter, Peixiang Lu, Aron Walsh, and Anthony K Cheetham. Unusual phase transition driven by vibrational entropy changes in a hybrid organic-inorganic perovskite. *Angewandte Chemie International Edition*, 2018.
- [47] Sungwon Kim, Venkatraman Gopalan, and Alexei Gruverman. Coercive fields in ferroelectrics: A case study in lithium niobate and lithium tantalate. *Applied Physics Letters*, 80(15):2740–2742, 2002.
- [48] HF Wang, YY Zhu, SN Zhu, and NB Ming. Investigation of ferroelectric coercive field in  $\text{LiNbO}_3$ . *Applied Physics A: Materials Science & Processing*, 65(4):437–438, 1997.
- [49] Y Nahas, S Prokhorenko, and I Kornev. Interplay between pressure and local symmetry in  $(\text{Pb}_{1-3/2x}\text{La}_x)(\text{Zr}_{60}\text{Ti}_{40})\text{O}_3$ : Emergence of a relaxor state. *Physical Review B*, 90(18):180102, 2014.
- [50] W Kleemann, J Dec, P Lehnert, R Blinc, B Zalar, and R Pankrath. Uniaxial relaxor ferroelectrics: The ferroic random-field Ising model materialized at last. *EPL (Europhysics Letters)*, 57(1):14, 2002.
- [51] A Bussmann-Holder and AR Bishop. Intrinsic local modes and heterogeneity in relaxor ferroelectrics. *Journal of Physics: Condensed Matter*, 16(25):L313, 2004.
- [52] AA Bokov and Z-G Ye. Recent progress in relaxor ferroelectrics with perovskite structure. In *Frontiers of Ferroelectricity*, pages 31–52. Springer, 2006.
- [53] Hiroyuki Takenaka, Ilya Grinberg, Shi Liu, and Andrew M Rappe. Slush-like polar structures in single-crystal relaxors. *Nature*, 546(7658):391, 2017.
- [54] Y Nahas and I Kornev. Local symmetry approach to relaxor ferroelectrics. *EPL (Europhysics Letters)*, 103(3):37013, 2013.
- [55] Marcel Porta, Turab Lookman, and Avadh Saxena. Effects of criticality and disorder on piezoelectric properties of ferroelectrics. *Journal of Physics: Condensed Matter*, 22(34):345902, 2010.
- [56] Julien Haines, O Cambon, N Prudhomme, Guillaume Fraysse, DA Keen, LC Chapon, and MG Tucker. High-temperature, structural disorder, phase transitions, and piezoelectric properties of  $\text{GaPO}_4$ . *Physical Review B*, 73(1):014103, 2006.
- [57] Badari Narayana Rao, Ranjan Datta, S Selva Chandrashekaran, Dileep K Mishra, Vasant Sathe, Anatoliy Senyshyn, and Rajeev Ranjan. Local structural disorder and its influence on the average global structure and polar properties in  $\text{Na}_{0.5}\text{Bi}_{0.5}\text{TiO}_3$ . *Physical Review B*, 88(22):224103, 2013.
- [58] I Ponomareva and S Lisenkov. Bridging the macroscopic and atomistic descriptions of the electrocaloric effect. *Physical review letters*, 108(16):167604, 2012.
- [59] L Shebanovs, K Borman, WN Lawless, and A Kalvane. Electrocaloric effect in some perovskite ferroelectric ceramics and multilayer capacitors. *Ferroelectrics*, 273(1):137–142, 2002.
- [60] MJ Krogstad, PM Gehring, S Rosenkranz, R Osborn, F Ye, Y Liu, JPC Ruff, W Chen, JM Wozniak, H Luo, et al. The relation of local order to material properties in relaxor ferroelectrics. *Nature Materials*, page 1, 2018.
- [61] Miroslava Schaffer, Bernhard Schaffer, and Quentin Ramasse. Sample preparation for atomic-resolution STEM at low voltages by FIB. *Ultramicroscopy*, 114:62–71, 2012.
- [62] Colin Ophus, Jim Ciston, and Chris T Nelson. Correcting non-linear drift distortion of scanning probe and scanning transmission electron microscopies from image pairs with orthogonal scan directions. *Ultramicroscopy*, 162:1–9, 2016.
- [63] Xavier Gonze, Fran ois Jollet, F Abreu Araujo, Donat Adams, Bernard Amadon, Thomas Appelcourt, Christophe Audouze, J-M Beuken, Jordan Bieder, A Bokhanchuk, et al. Recent developments in the ABINIT software package. *Computer Physics Communications*, 205:106–131, 2016.
- [64] Eberhard KU Gross and Reiner M Dreizler. *Density functional theory*, volume 337. Springer Science & Business Media, 2013.
- [65] Pierre Hohenberg and Walter Kohn. Inhomogeneous electron gas. *Physical review*, 136(3B):B864, 1964.
- [66] Xavier Gonze, Bernard Amadon, P-M Anglade, J-M Beuken, Fran ois Bottin, Paul Boulanger, Fabien Bruneval, Damien Caliste, Razvan Caracas, Michel C te, et al. Abinit: First-principles approach to material and nanosystem properties. *Computer Physics Communications*, 180(12):2582–2615, 2009.
- [67] John P Perdew, Adrienn Ruzsinszky, G bor I Csonka, Oleg A Vydrov, Gustavo E Scuseria, Lucian A Constantin, Xiaolan Zhou, and Kieron Burke. Restoring the density-gradient expansion for exchange in solids and surfaces. *Physical Review Letters*, 100(13):136406, 2008.
- [68] Miguel AL Marques, Micael JT Oliveira, and Tobias Burnus. Libxc: A library of exchange and correlation functionals for density functional theory. *Computer Physics Communications*, 183(10):2272–2281, 2012.
- [69] Michiel van Setten, Matteo Giantomassi, Eric Bousquet, Matthieu J Verstraete, Donald R Hamann, Xavier Gonze, and Gian-Marco Rignanese. The PseudoDojo: Training and grading a 85 element optimized norm-conserving pseudopotential table. *Computer Physics Communications*, 2018.
- [70] DR Hamann. Optimized norm-conserving Vanderbilt pseudopotentials. *Physical Review B*, 88(8):085117, 2013.
- [71] Fernando Casas, Ander Murua, and Mladen Nadinic. Efficient computation of the Zassenhaus formula. *Computer Physics Communications*, 183(11):2386–2391, 2012.
- [72] Hendrik J Monkhorst and James D Pack. Special points for brillouin-zone integrations. *Physical review B*, 13(12):5188, 1976.
- [73] Xavier Gonze and Changyol Lee. Dynamical matrices, Born effective charges, dielectric permittivity tensors, and interatomic force constants from density-functional perturbation theory. *Physical Review B*, 55(16):10355, 1997.
- [74] Izumi Tomono and Sadao Matsumura. Elastic and dielectric properties of  $\text{LiNbO}_3$ . *Journal of the Physical Society of Japan*, 56(1):163–177, 1987.
- [75] Michael A O’Keefe and Roar Kilaas. Advances in high-resolution image simulation. 1988.